



The University of  
**Nottingham**

UNITED KINGDOM · CHINA · MALAYSIA

Mahmoud, Hanafy and Al-Timimy, A. and Degano, Michele and Di Nardo, Mauro and Bianchi, Nicola and Gerada, C. (2017) Axial eccentric SynRel and SPM Motors analytical models validation using 3D finite element. In: SDEMPED 2017 - IEEE 11th International Symposium on Diagnostics for Electrical Machines, Power Electronics and Drives, 29 Aug - 1 Sept 2017, Tinos, Greece.

**Access from the University of Nottingham repository:**

<http://eprints.nottingham.ac.uk/52314/1/Axial%20Eccentric%20SynRel%20and%20SPM%20Motors%20Analytical.pdf>

**Copyright and reuse:**

The Nottingham ePrints service makes this work by researchers of the University of Nottingham available open access under the following conditions.

This article is made available under the University of Nottingham End User licence and may be reused according to the conditions of the licence. For more details see:  
[http://eprints.nottingham.ac.uk/end\\_user\\_agreement.pdf](http://eprints.nottingham.ac.uk/end_user_agreement.pdf)

**A note on versions:**

The version presented here may differ from the published version or from the version of record. If you wish to cite this item you are advised to consult the publisher's version. Please see the repository url above for details on accessing the published version and note that access may require a subscription.

For more information, please contact [eprints@nottingham.ac.uk](mailto:eprints@nottingham.ac.uk)

# Axial Eccentric SynRel and SPM Motors Analytical Models Validation Using 3D Finite Element

H. Mahmoud, A. Al-Timimy, M. Degano, M. Di Nardo, N. Bianchi, and C. Gerada

**Abstract**—This paper deals with the uniform and non-uniform axial eccentricity analyses of the surface mounted permanent magnet and synchronous reluctance machines. The analyses are carried out using an analytical model for each considered machine. Being the axial eccentricity a 3D physical phenomenon, the standard sliding approach used in the analytical models has been validated through accurate 3D FE simulations. The results presented in this paper verify the effectiveness of the analytical approaches quantifying the results deviations respect to the computational expensive 3D FE simulations. The results also confirms that synchronous reluctance machines show higher radial forces compared to the surface permanent magnet machines for the same eccentricity level, main geometry and operating condition.

**Index Terms**—Non-uniform axial eccentricity, Uniform axial eccentricity, Analytical analysis, 3D finite element modelling.

## I. INTRODUCTION

Both permanent magnet (SPM) and synchronous reluctance (SynRel) machines are widely used for their respective merits in several low-medium speed applications, such as industrial, traction, household, etc. [1], [2]. The SPM machines, which make use of high energy density permanent magnets (PMs), show the highest torque density and efficiency. However the use of rare earth based PMs is also the root of the main disadvantage of this machine topology, i.e. its high cost [2]–[4]. Consequently both academia and industries have attempted to reduce the use of rare earth PMs both by optimizing the SPM design or adopting other machine topologies. Another design challenge of SPM machines widely addressed in literature regards the reduction of the cogging torque which can be faced applying several methods [5]–[8].

The interest towards SynRel machines in the last years is justified by its torque density, comparable to the induction motor one, and the absence of rare earth PMs and so its lower and more stable cost [9], [10]. High torque ripple and low power factor are the most important disadvantages of SynRel machines. The first one can be greatly reduced by properly designing the rotor geometry [11]–[14], while the power factor can be significantly increased by inserting small amount of PMs (also rare earth free materials such as Ferrite PMs) inside the rotor flux barriers [10], [15].

H. Mahmoud, A. Al-Timimy, M. Degano, M. Di Nardo, and C. Gerada are with the Department of Electrical and Electronic Engineering, University of Nottingham, NG72RD, Nottingham, Uk, M. Degano and C. Gerada are also with the Department of Electrical and Electronic Engineering, University of Ningbo China, Ningbo, China, Hanafy.Mahmoud@nottingham.ac.uk, Ahmed.Al-Timimy@nottingham.ac.uk, mauro.dinardo@nottingham.ac.uk and michele.degano@nottingham.ac.uk.

N. Bianchi is with the Department of Industrial Engineering, University of Padova, Via Gradenigo, 6A, 35131 Padova (Italy), nicola.bianchi@unipd.it.

A relevant amount of literature has lately addressed the more "practical" problem of the worsening of the electromagnetic performance related with manufacturing and assembling processes. One of the possible root of performance alteration is due to the manufacturing tolerance of the bearing housings and the accuracy of the rotor/stator assembly [16], [17].

The latter mainly causes the rotor axis to be not perfectly placed on the stator axis. In particular, Fig. 1 (a) shows an axially non-uniform eccentricity in which only one end of the machine is eccentric, Fig. 1 (b) displays an axially non-uniform eccentricity in which both ends of the motor are equally eccentric, and Fig. 1 (c) reports an axially uniform displacement of the rotor axis with respect to the stator axis. Besides, the above described geometrical cases, the axis of rotation can coincide with the rotor axis or with the stator axis. The first case is called static eccentricity while the second is the dynamic eccentricity [18], [19]; a combination of both cases can obviously occur.

The effect of all the above described eccentricity cases for SPM machines have been widely addressed in [20], while the same analyses on the SynRel machines have not received the same attention. In particular, late studies [21], [22] have analysed the axially uniform eccentricity on SynRel machines. In [20], [23], also the non-uniform axial eccentricity effect on both SPM and SynRel machines have been investigated subdividing the rotor axial length into a finite number of slides. The respective analytical or 2D FE model is then applied to each axial slide and consequently the total magnetic force caused by the eccentricity can be computed.

Being the non-uniform axial eccentricity a 3D physical phenomenon, it is important to compare the sliding approach used in the analytical models (and in the 2D FE) through an accurate 3D FE simulation. Therefore, this paper focuses on the 3D modelling of both machines in different axial eccentricity cases shown in Fig. 1. The developed comparative study, carried out on both machines, allows determining the accuracy of both 2D analytical model and 2D FE solution with respect to the more complex and time consuming 3D FE simulation. The paper structure is as following: (a) section II briefly describes the 2D analytical models of both eccentric machines, (b) section III shows the 3D modelling of the both machines in the three different cases of rotor axial displacement, and (c) section IV presents the comparison between the results of the 3D and the 2D models, as well as, between the two eccentric machines.

## II. THE 2D ANALYTICAL MODELS

The non-uniform air-gap thickness distribution, results from eccentricity, affects the air-gap flux density distribution. Con-

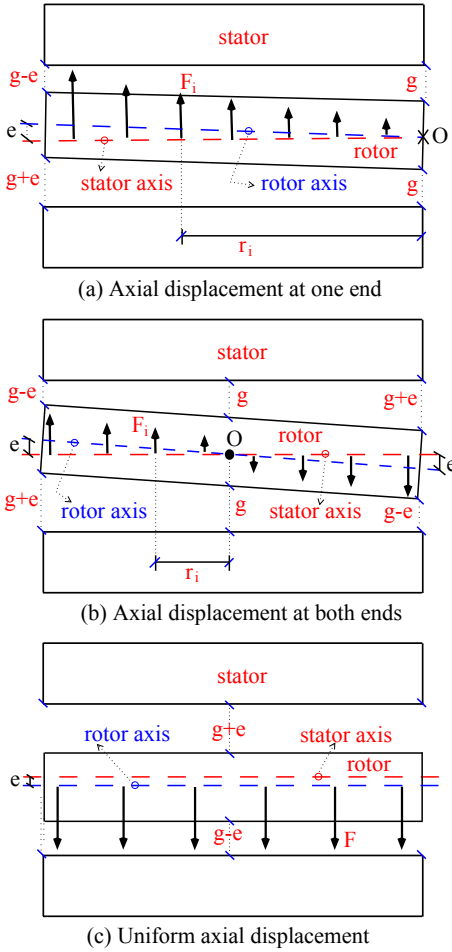


Fig. 1: Side view of an electric motor shows the three different axial eccentricity cases.

sequently the magnetic radial pressure on the rotor periphery becomes asymmetric leading to an unbalanced magnetic force acting on the rotor.

The mathematical expression describing the non-uniform air-gap length, in case of static eccentricity, was firstly proposed in [24]–[26]. Analysing Fig. 2, it can be recognized that the minimum air-gap length is fixed with the rotor rotation. Thus, the air-gap length variation does not depend on the rotor position and can be expressed as:

$$g(\theta_s) = g - e \cos(\theta_s) = g[1 - \Delta \cos(\theta_s - \theta_e)] \quad (1)$$

where  $e$  is the eccentricity distance between the stator axial center and the rotor axial center,  $\Delta = e/g$  is the relative eccentricity, given by the ratio of the rotor displacement and the air-gap,  $\theta_e$  and  $\theta_s$  are the initial angle of the eccentricity and the coordinate angle referring to the stator stationary reference frame (mechanical degrees), respectively.

In case of dynamic eccentricity, the analytical formulation of the air-gap length as function of the rotor position has been first presented in [27]. In particular, it can be geometrically derived analyzing Fig. 3, as

$$g(\theta_s) = g - e \cos(\theta_s - \theta_m) = g[1 - \Delta \cos(\theta_s - \theta_m - \theta_e)] \quad (2)$$

where  $\theta_m$  is the rotor position angle (mechanical degrees).

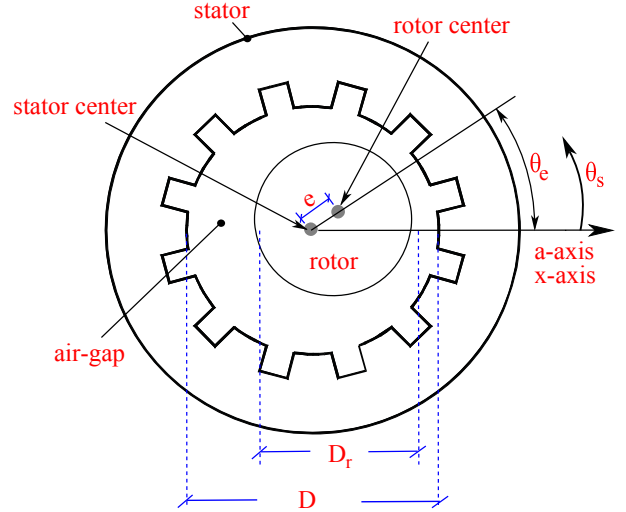


Fig. 2: Air-gap length variation with the rotor rotation, in case of static eccentricity.

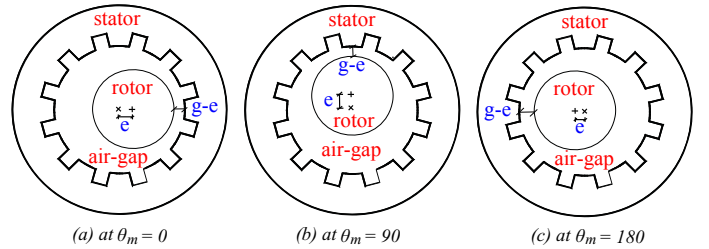


Fig. 3: Air-gap length variation with the rotor rotation, in case of dynamic eccentricity, with  $\theta_e = 0^\circ$ .

In the following, the influence of such variation on the computation of the air-gap flux density distribution is discussed on both SynRel and SPM motors.

#### A. Eccentric SynRel machine

As reported in [21], from the equivalent magnetic network, the flux density distribution in the air-gap is computed as

$$B_g(\theta_s) = \mu_o \frac{-U_s(\theta_s) + U_r(\theta_s)}{g(\theta_s)} \quad (3)$$

where  $U_s(\theta_s)$  and  $U_r(\theta_s)$  are the stator and rotor scalar magnetic potential distributions, respectively. Their computations are illustrated in details in [21], [23].

As highlighted in [21], the computation of the rotor scalar magnetic potential, and hence,  $B_g(\theta_s)$  requires to integrate the expression shown in (3). However, in eccentricity case, the symbolic integration of  $B_g(\theta_r)$  is complicated due to the cosine function in the denominator. Therefore, with the aim of simplifying this integration, the air-gap is split into different regions. Then, the integration is implemented on each region considering the average of air-gap length variation in each region ( $\bar{g}$ ), i.e., as a constant value. The number of these regions ( $n_g$ ) depends on the number of pole pairs ( $p$ ) and number of flux-barriers per pole ( $N_b$ ). It can be expressed as

$$n_g = 4N_b p \quad (4)$$

The generic expression of the average air-gap length over a region boarded by the angles  $(\gamma_1$  and  $\gamma_2)$  is called  $\bar{g}_{\gamma_1 \rightarrow \gamma_2}$ . In static eccentricity case, considering  $\theta_e = 0^\circ$ ,  $\bar{g}_{\gamma_1 \rightarrow \gamma_2}$  is computed related to the stator reference frame as

$$\bar{g}_{\gamma_1 \rightarrow \gamma_2} = g \left[ 1 - \frac{2\Delta}{\gamma_2 - \gamma_1} \cos\left(\frac{\gamma_1 + \gamma_2}{2}\right) \sin\left(\frac{\gamma_2 - \gamma_1}{2}\right) \right] \quad (5)$$

Similarly,  $\bar{g}_{\gamma_1 \rightarrow \gamma_2}$ , in case of dynamic eccentricity, in the stator stationary reference frame, is expressed as

$$\bar{g}_{\gamma_1 \rightarrow \gamma_2} = g \left[ 1 - \frac{2\Delta}{\gamma_2 - \gamma_1} \cos\left(\frac{\gamma_1 + \gamma_2}{2} - \theta_m\right) \sin\left(\frac{\gamma_2 - \gamma_1}{2}\right) \right] \quad (6)$$

### B. Eccentric SPM machine

Analyzing Fig. 4, which shows a cross section of an eccentric SPM machine, it can be deduced that the air-gap length variation can be expressed by the variation of the internal radius of the stator according to the rotor center  $R_{sr}(\theta_s)$ .

The air-gap flux density  $B_g(\theta_s)$  can be computed using the model presented in [20] in case of concentric machine. In such healthy case, the air-gap flux density depends on the stator inner radius  $R_s$ . By simply replacing  $R_s$  with  $R_{sr}$ , it is possible to determine  $B_g(\theta_s)$  also for the eccentric machine using the same analytical model. The stator radius in the new reference frame can be computed from  $R_s$  and the angle  $\theta_s$ . In particular, considering a generic point  $P$  on the stator periphery, its Cartesian coordinates in the stator reference frame are given by:

$$P_{xs} = R_s \cos(\theta_s) \quad \text{and} \quad P_{ys} = R_s \sin(\theta_s) \quad (7)$$

Hence, the coordinates of point  $P$  at rotor reference are computed as

$$P_{xr} = P_{xs} - e \quad \text{and} \quad P_{yr} = P_{ys} \quad (8)$$

Then,  $R_{sr}$  and  $\theta_{sr}$  are given by:

$$R_{sr} = \sqrt{P_{xr}^2 + P_{yr}^2} \quad \text{and} \quad \theta_{sr} = \tan^{-1}(P_{yr}/P_{xr}) \quad (9)$$

Finally,  $R_{sr}(\theta_{sr})$  can be computed for  $\theta_{sr}$  varying from  $0^\circ$  to  $360^\circ$  which cover the air-gap length variation.

The radial magnetic pressure and force on the overall rotor, in case of uniform axial eccentricity, can be computed, as reported in [21].

### C. Sliding approach

As mentioned in the introduction, the computation of the radial forces in case of non-uniform axial eccentricity of both machines can be carried adopting the sliding approach. The latter simply consists in sub-dividing the rotor into a finite number of axial slides [20], [21], [23]. As a consequent, the eccentricity of each rotor slide can be considered as uniform axial eccentricity, and hence, the force can be easily computed using the above described analytical models. Once the radial forces on each axial slides have been calculated, the total force is simply the sum of all the forces. The same sliding approach is used with the 2D FE models. Thus, it is important to implement the 3D FE modelling to validate the results of both 2D analytical and FE models, specially in case of non-uniform axial eccentricity.

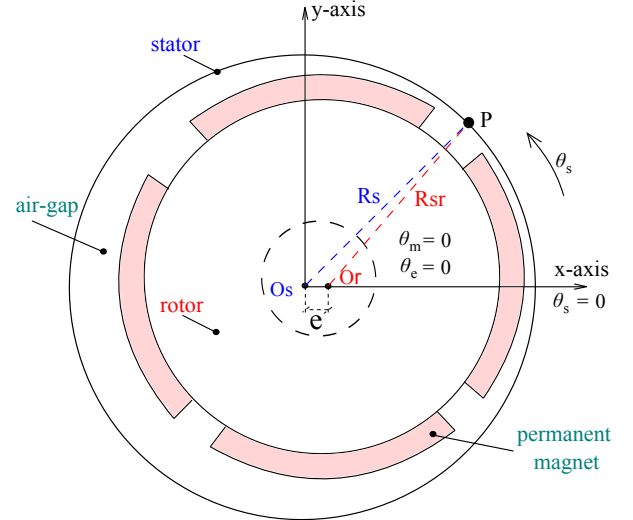


Fig. 4: Cross section of eccentric SPM machine.

## III. 3D FINITE ELEMENT ANALYSIS

The eccentricity of both SynRel and SPM machines have been simulated via 3D FE analysis since it allows considering the non-uniform axial displacement without neglecting any electromagnetic components (such as the end winding). The use of 3D FE analysis is usually discouraged due to the extremely high computational cost and to the long time required to set up the model [28]. The FE analyses have been obviously carried out replicating as much as possible the hypotheses of the analytical modeling, i.e. the stator replaced by an equivalent current sheet, an infinite iron permeability. These assumptions lead to simplify the 3D FE models of both machines, as shown in Fig. 5, and reduce the simulation time.

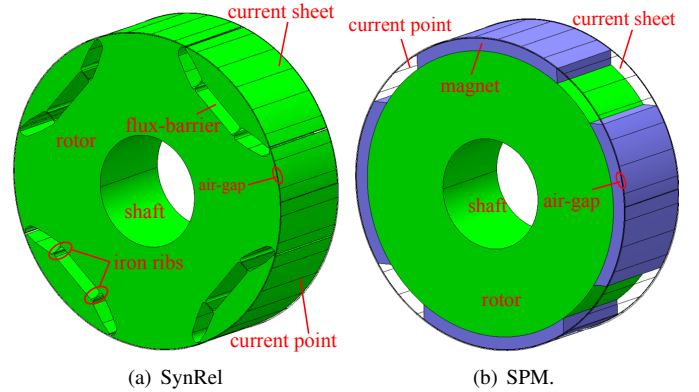


Fig. 5: 3D Cross-section of (a) SynRel and (b) SPM motors.

Fig. 5 shows the 3D cross-section of the two machine topologies while the generated 3D-mesh of both machines rotors are presented in Fig. 6.

Although the stator geometry is not considered, the creation of the mesh in the air-gap region in case of eccentric machines, it is a critical part of the 3D FE modelling therefore it requires particular attention. In order to improve the accuracy of the magnetic field computation in the air-gap (being the zone

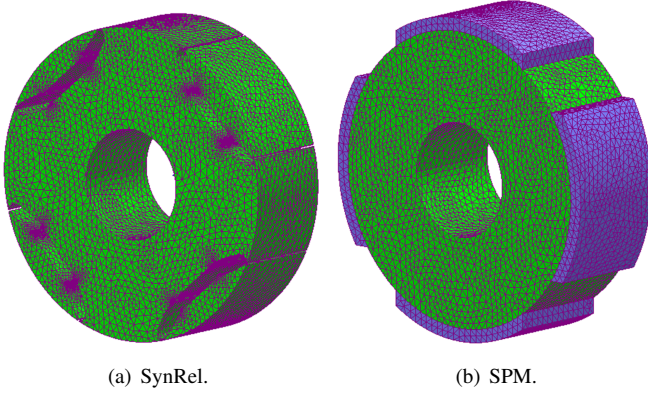


Fig. 6: Mesh density map of (a) SynRel and (b) SPM motors.

with the highest energy density), it is a common practice to subdivide this component into several layers (i.e. hollow concentric cylinders) and impose the mesh vertexes on the peripheries of such layers. In this case, the air-gap has been divided into four layers as shown in Fig. 7 (a) for the concentric case, as recommended by the adopted FE suit [29].

In the case of concentric machines, the thicknesses of each air-gap layer are simply all equal to each other, i.e.  $d = g / 4$ . However in case of eccentric machines, the thickness of each air-gap layer  $d_i$  has to be properly calculated in order to avoid the overlapping of two or more components. The easiest way to avoid this modelling problem is to consider the three air-gap layers nearer to the rotor with an equal thickness of  $d_i = (g - e) / 4$ . By doing so, the three inner air-gap layers will feature a constant thickness and only the outer one will have a non-constant thickness reaching a minimum of  $d_i$  (so bigger than zero) in the point where the air-gap is minimum. The mesh at the maximum and minimum air-gap lengths are shown in Fig. 7 (b) and Fig. 7 (c) for the sake of clarity.

Regarding the implementation of the axially non-uniform eccentricity, to simplify the modelling, instead of moving the rotor within the stator, it has been decided to fix the rotor and move the stator current sheet (defined by a lower number of points). Fig. 8 clarifies how the current sheet has been moved in the eccentricities cases depicted in Fig. 1.

#### IV. RESULTS COMPARISON

This section presents the results of the 2D analytical models of both SynRel and SPM motors at the different axial eccentricity scenarios. The results of both models are validated by both 2D and 3D FE analyses. In addition, the two machines are compared together in the aforementioned three eccentricity cases. For fair comparison, the two machines have the same main stator geometry, i.e.,  $Q_s$ ,  $L_{stk}$ ,  $p$ , and  $g$ . Table. I and Table. II report the main geometrical data of SynRel and SPM motor, respectively. For the following analysis, the eccentricity  $e$  is set equal to 0.2.

Fig. 9 and Fig. 10 show the 3D flux density map of the SynRel and SPM motors at the rated speed, in case of no eccentricity. It is noted that there is a symmetric distribution of

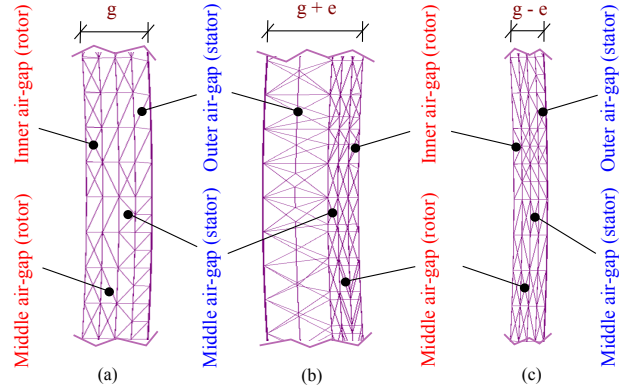


Fig. 7: Mesh in (a) the uniform air-gap length, i.e., healthy case, (b) the maximum air-gap length in case of eccentricity, and (c) the minimum air-gap length in case of eccentricity, respectively.

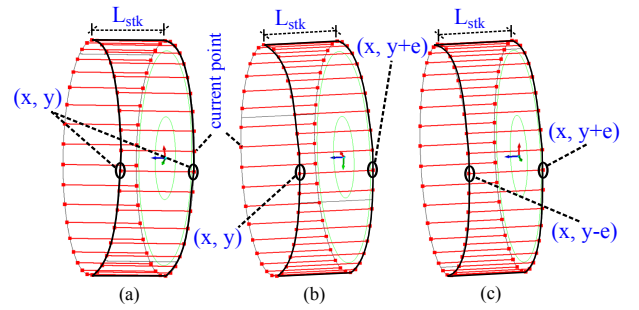


Fig. 8: The current sheet in case of (a) uniform axial displacement and non-uniform axial displacement between the rotor and stator axes at (b) one end and (c) both ends.

TABLE I: The main geometrical data of the both machine.

$g$	0.35 mm
$R_s$	62.5 mm
$R_r$	62.15 mm
$L_{stk}$	40 mm
$p$	4
$Q_s$	36

TABLE II: Geometrical data of the SPM machine.

$t_{sleev}$	0.15 mm
$g_{spm} = g + t_{sleev}$	0.5 mm
$R_s$	62.5 mm
$R_m$	62 mm
$h_m$	5 mm
$R_r$	57 mm
$\alpha_p$	0.67
$B_{rem}$	0.905 T

the flux density for both motors, as highlighted by the dotted circles in both figures. As expected, the radial force on the overall rotor is equal to zero.

##### A. Uniform axial displacement

Fig. 11 and Fig. 12 show the 3D flux density maps of both motors. It is worth noticing that the flux density is higher in the area where the air-gap is minimum (right side of the figure). Obviously the flux density is uniform along the axial length of both motors.



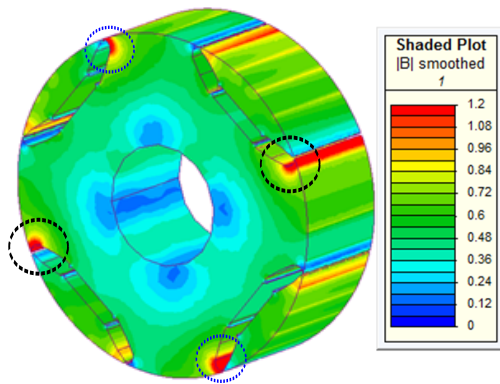


Fig. 9: 3D Flux density map of concentric SynRel motor.

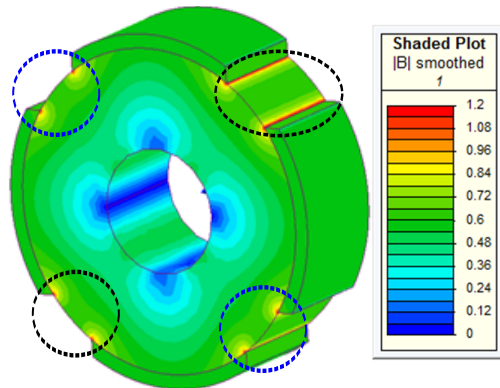


Fig. 10: 3D Flux density map of concentric SPM motor.

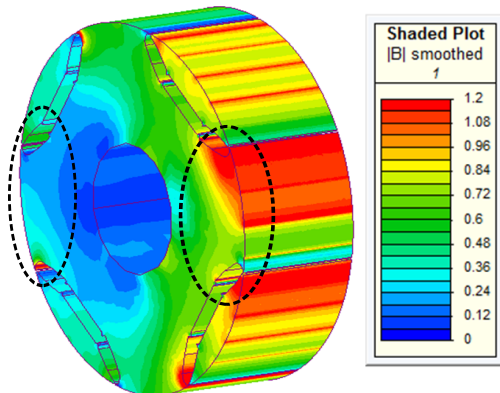


Fig. 11: 3D Flux density map of SynRel motor in case of uniform axial eccentricity at the right hand side.

The air-gap flux density distribution, resulted from the analytical, 2D and 3D FE models of both motors, are compared together, as shown in Fig. 13 and Fig. 14. It is noted that there are good agreement between the results of both analytical models and their corresponding 2D and 3D FE analyses.

Fig. 15 and Fig. 16 show the radial magnetic force acting on the rotor of both motors under no-load and load operating conditions. Also these figures show a satisfactory agreement between the analytical models of the two motors and their corresponding 2D and 3D FE analyses. Comparing the radial forces on the rotor of both motors, shown in Fig. 15 and Fig. 16, it is recognized that the SynRel is worsen than the

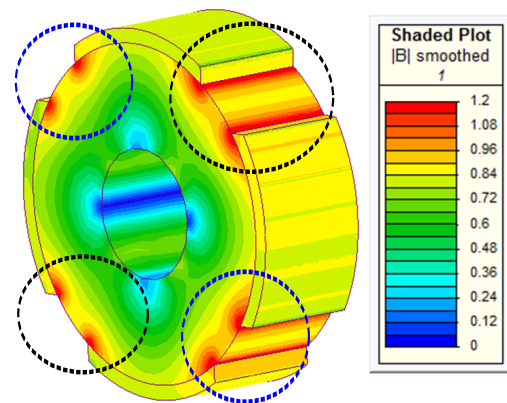


Fig. 12: 3D Flux density map of SPM motor in case of uniform axial eccentricity at the right hand side.

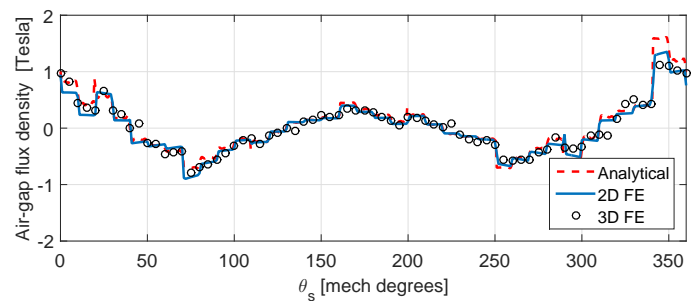


Fig. 13: Air-gap flux density distribution of SynRel motor in case of uniform axial eccentricity at the right hand side.

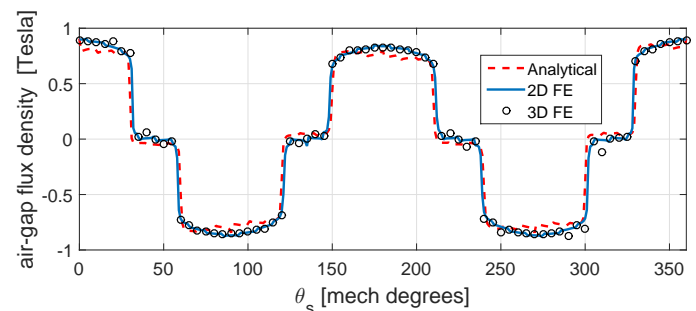


Fig. 14: Air-gap flux density distribution of SPM motor in case of uniform eccentricity at the right hand side.

SPM motor, in case of uniform axial eccentricity.

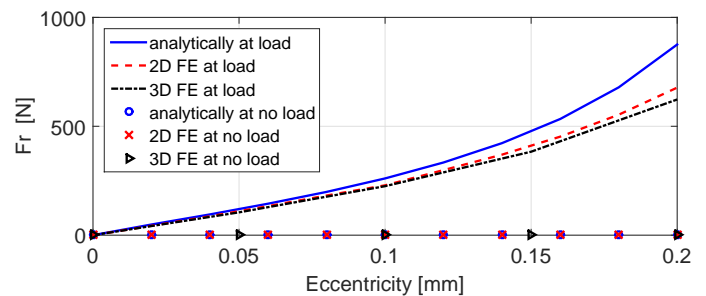


Fig. 15: Radial magnetic force acting on the rotor of SynRel motor in case of uniform eccentricity at the right hand side.

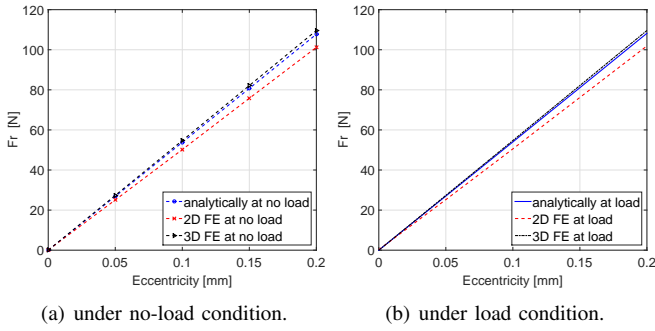


Fig. 16: Radial magnetic force acting on the rotor of SPM motor in case of uniform eccentricity at the right hand side under (a) no-load and (b) load conditions.

### B. Non-uniform axial displacement

As highlighted in Fig. 1 (a) and Fig. 1 (b), the air-gap length exhibits non-uniform distribution through the axial length of the motor. Thus, the axial air-gap flux density distribution is non-uniform. The suitable presentation of this flux density variation is the 3D flux density map.

1) *at one end*: Fig. 17 and Fig. 18 show the 3D flux density maps of SynRel and SPM motors, respectively. Referring to the dotted circle shown in the upper parts of the two maps, the flux density is high at the minimum air-gap length, i.e.  $g - e$ , and is gradually reduced through the axial length till the desired air-gap length  $g$ . In addition, regarding to the lower part of both motors, the flux density is low at air-gap length equal to  $g + e$ , then it is increased gradually till reach the flux density of the healthy case, i.e., at air-gap length equal to  $g$ .

The radial magnetic forces acting on the rotors of both motors are computed from the analytical models, 2D and 3D FE analyses, as shown in Fig. 19 and Fig. 20. Once again, a good agreement between the analytical models and the FE analyses is achieved.

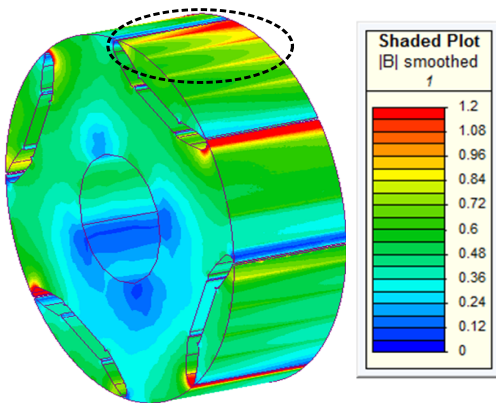


Fig. 17: 3D Flux density map of SynRel motor in case of non-uniform axial displacement at one end.

2) *at both ends*: Similarly, the 3D flux density maps of SynRel and SPM motors are shown in Fig. 21 and Fig. 22, respectively. For the upper part of both motors, it is noted that

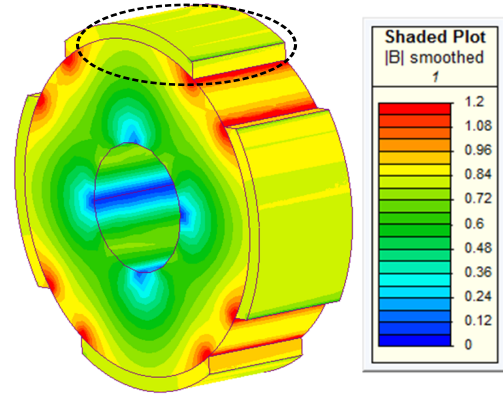


Fig. 18: 3D Flux density map of SPM motor in case of non-uniform axial displacement at one end.

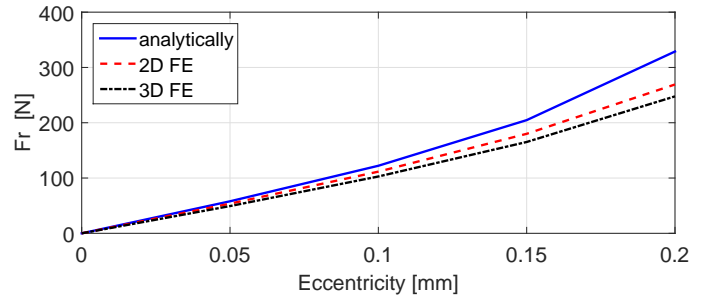


Fig. 19: Radial magnetic force acting on the rotor of SynRel motor in case of non-uniform axial displacement at one end.

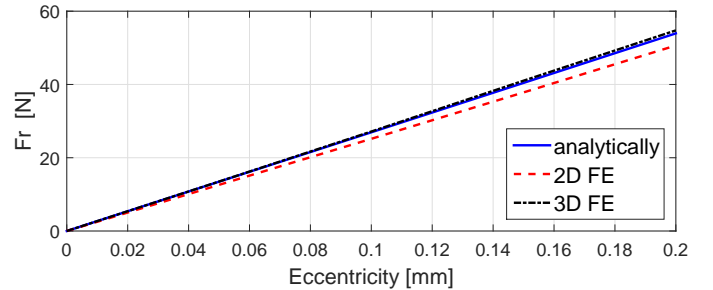


Fig. 20: Radial magnetic force acting on the rotor of SPM motor in case of non-uniform axial displacement at one end.

the flux density exhibits its maximum value at air-gap length equal to  $g - e$ , then it is gradually reduced to its minimum value at air-gap length equal to  $g + e$ . The contrary is recognised for the lower parts of both motors.

As expected the radial forces acting on the rotor of both machines in case of non-uniform axial displacement at both ends is equal to zero.

## V. CONCLUSIONS

This paper shows two rapid analytical models of both SynRel and SPM motors. These models are not only valid for healthy (no eccentricity) case, but also for the different axial eccentricity cases. The 2D FE analyses are enough to confirm the results of both analytical models at the uniform axial eccentricity case. However, the sliding approach used

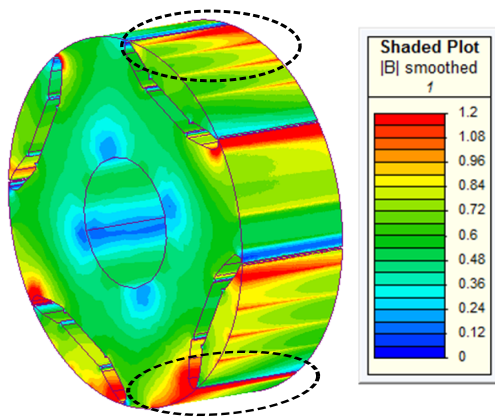


Fig. 21: 3D Flux density map of SynRel motor in case of non-uniform axial displacement at both ends.

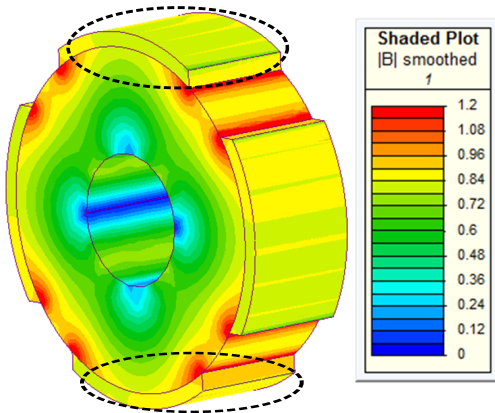


Fig. 22: 3D Flux density map of SPM motor in case of non-uniform axial displacement at both ends.

with both analytical models, in case of non-uniform axial eccentricity, is validated by the 3D FE analyses.

The axial flux density variations of both motor are illustrated by 3D maps at the different eccentricity cases. In addition, it is noted that the radial forces estimated by the analytical models have good agreement with those resulted from both 2D and 3D FE analyses. Finally, the results of the two analytical models are compared together in order to decide which motor is the worst in the different eccentricity cases. As expected, it can be concluded that the SynRel motor is the worst at all cases of eccentricity.

#### REFERENCES

- [1] G. Pellegrino, A. Vagati, P. Guglielmi, and B. Boazzo, "Performance comparison between surface-mounted and interior PM motor drives for electric vehicle application," *IEEE Transactions on Industrial Electronics*, vol. 59, no. 2, pp. 803–811, Feb 2012.
- [2] A. Vagati, B. Boazzo, P. Guglielmi, and G. Pellegrino, "Design of ferrite-assisted synchronous reluctance machines robust toward demagnetization," *IEEE Transactions on Industry Applications*, vol. 50, no. 3, pp. 1768–1779, May 2014.
- [3] P. Guglielmi, B. Boazzo, E. Armando, G. Pellegrino, and A. Vagati, "Permanent-magnet minimization in PM-Assisted synchronous reluctance motors for wide speed range," *IEEE Transactions on Industry Applications*, vol. 49, no. 1, pp. 31–41, Jan 2013.
- [4] B. Boazzo, A. Vagati, G. Pellegrino, E. Armando, and P. Guglielmi, "Multipolar ferrite-assisted synchronous reluctance machines: A general design approach," *IEEE Transactions on Industrial Electronics*, vol. 62, no. 2, pp. 832–845, Feb 2015.
- [5] Z. Q. Zhu and D. Howe, "Influence of design parameters on cogging torque in permanent magnet machines," in *Conference Record of IEEE International Electric Machines and Drives*, May 1997, pp. MA1/3.1–MA1/3.3.

- [6] N. Bianchi and S. Bolognani, "Design techniques for reducing the cogging torque in surface-mounted PM motors," *IEEE Transactions on Industry Applications*, vol. 38, no. 5, pp. 1259–1265, Sep 2002.
- [7] L. Dosiek and P. Pillay, "Cogging torque reduction in permanent magnet machines," *IEEE Transactions on Industry Applications*, vol. 43, no. 6, pp. 1565–1571, Nov 2007.
- [8] N. Chen, S. L. Ho, and W. N. Fu, "Optimization of permanent magnet surface shapes of electric motors for minimization of cogging torque using fem," *IEEE Transactions on Magnetics*, vol. 46, no. 6, pp. 2478–2481, June 2010.
- [9] M. Barcaro and N. Bianchi, "Interior PM machines using ferrite to substitute rare-earth surface pm machines," in *2012 XXth International Conference on Electrical Machines, Marseille, France*, Sept 2012, pp. 1339–1345.
- [10] N. Bianchi, H. Mahmoud, and S. Bolognani, "Fast synthesis of permanent magnet assisted synchronous reluctance motors," *IET Electric Power Applications*, vol. 10, no. 5, pp. 312–318, 2016.
- [11] A. Vagati, M. Pastorelli, G. Francheschini, and S. C. Petrache, "Design of low-torque-ripple synchronous reluctance motors," *IEEE Transactions on Industry Applications*, vol. 34, no. 4, pp. 758–765, Jul 1998.
- [12] D. Ionel, "Interior permanent magnet motor including rotor with unequal poles," *US Patent*, 8,102,091, 2102.
- [13] N. Bianchi, S. Bolognani, D. Bon, and M. D. Pre, "Rotor flux-barrier design for torque ripple reduction in synchronous reluctance and pm-assisted synchronous reluctance motors," *IEEE Transactions on Industry Applications*, vol. 45, no. 3, pp. 921–928, May 2009.
- [14] M. Degano, E. Carraro, and N. Bianchi, "Selection criteria and robust optimization of a traction PM-Assisted synchronous reluctance motor," *IEEE Transactions on Industry Applications*, vol. 51, no. 6, pp. 4383–4391, Nov 2015.
- [15] N. Bianchi and H. Mahmoud, "An analytical approach to design the PM in PMAREL motors robust toward the demagnetization," *IEEE Transactions on Energy Conversion*, vol. 31, no. 2, pp. 800–809, June 2016.
- [16] L. Gasparin and R. Fiser, "Intensity of the native and additional harmonic components in cogging torque due to design parameters of permanent-magnet motors," in *International Conference on Power Electronics and Drive Systems (PEDS), Taipei, Taiwan*, Nov 2009, pp. 1062–1067.
- [17] I. Coenen, M. van der Giet, and K. Hameyer, "Manufacturing tolerances: Estimation and prediction of cogging torque influenced by magnetization faults," *IEEE Transactions on Magnetics*, vol. 48, no. 5, pp. 1932–1936, May 2012.
- [18] H. Mahmoud and N. Bianchi, "Comparison between synchronous reluctance and interior permanent magnet motors with eccentricity," in *IEEE Workshop on Electrical Machines Design, Control and Diagnosis (WEMDCD), Torino, Italy*, March 2015, pp. 22–27.
- [19] —, "Comparison between synchronous machines with eccentricity: Reluctance and permanent magnets," in *International Symposium on Power Electronics, Electrical Drives, Automation and Motion (SPEEDAM), Capri, Italy*, June 2016, pp. 394–400.
- [20] M. Michon, R. C. Holehouse, K. Atallah, and J. Wang, "Unbalanced magnetic pull in permanent magnet machines," in *7th IET International Conference on Power Electronics, Machines and Drives (PEMD), Manchester, UK*, April 2014, pp. 1–6.
- [21] H. Mahmoud and N. Bianchi, "Eccentricity in synchronous reluctance motors part I: Analytical and finite-element models," *IEEE Transactions on Energy Conversion*, vol. 30, no. 2, pp. 745–753, June 2015.
- [22] —, "Eccentricity in synchronous reluctance motors-part II: Different rotor geometry and stator windings," *IEEE Transactions on Energy Conversion*, vol. 30, no. 2, pp. 754–760, June 2015.
- [23] —, "Analytical comparison of synchronous reluctance and surface permanent magnet machines with rotor eccentricity," in *IEEE Energy Conversion Congress and Exposition (ECCE)*, Sept 2015, pp. 1765–1772.
- [24] S. Swann, "Effect of rotor eccentricity on the magnetic field in the air-gap of a non-salient-pole machine," *Proceedings of the Institution of Electrical Engineers*, vol. 110, no. 5, pp. 903–915, May 1963.
- [25] A. Smith and D. Dorrell, "Calculation and measurement of unbalanced magnetic pull in cage induction motors with eccentric rotors. i. analytical model," *IEE Proceedings - Electric Power Applications*, vol. 143, no. 3, pp. 193–201, May 1996.
- [26] D. Dorrell, W. Thomson, and S. Roach, "Combined effects of static and dynamic eccentricity on airgap flux waves and the application of current monitoring to detect dynamic eccentricity in 3-phase induction motors," in *Seventh International Conference on (Conf. Publ. No. 412) in Electrical Machines and Drives*, Sep 1995, pp. 151–155.
- [27] G. Joksimovic, M. Durovic, J. Penman, and N. Arthur, "Dynamic simulation of dynamic eccentricity in induction machines-winding function approach," *IEEE Transactions on Energy Conversion*, vol. 15, no. 2, pp. 143–148, June 2000.
- [28] L. Chen, J. Wang, and S. S. Nair, "An analytical method for predicting 3D eddy current loss in permanent magnet machines based on generalized image theory," *IEEE Transactions on Magnetics*, vol. 52, no. 6, pp. 1–11, June 2016.
- [29] "http://www.infolytica.com/en/products/magnet/!"